

# Impact of signal-to-noise ratio in a hyperspectral sensor on the accuracy of biophysical parameter estimation in case II waters

Wesley J. Moses,<sup>1,\*</sup> Jeffrey H. Bowles,<sup>2</sup> Robert L. Lucke,<sup>2</sup> and Michael R. Corson<sup>2</sup>

<sup>1</sup>National Research Council/Naval Research Laboratory Research Associate, Washington, D.C., USA

<sup>2</sup>Naval Research Laboratory, Washington, D. C., USA

\*wesley.moses.ctr.in@nrl.navy.mil

**Abstract:** Errors in the estimated constituent concentrations in optically complex waters due solely to sensor noise in a spaceborne hyperspectral sensor can be as high as 80%. The goal of this work is to elucidate the effect of signal-to-noise ratio (SNR) on the accuracy of retrieved constituent concentrations. Large variations in the magnitude and spectral shape of the reflectances from coastal waters complicate the impact of SNR on the accuracy of estimation. Due to the low reflectance of water, the actual SNR encountered for a water target is usually quite lower than the prescribed SNR. The low SNR can be a significant source of error in the estimated constituent concentrations. Simulated and measured at-surface reflectances were used in this study. A radiative transfer code, Tafkaa, was used to propagate the at-surface reflectances up and down through the atmosphere. A sensor noise model based on that of the spaceborne hyperspectral sensor HICO was applied to the at-sensor radiances. Concentrations of chlorophyll-*a*, colored dissolved organic matter, and total suspended solids were estimated using an optimized error minimization approach and a few semi-analytical algorithms. Improving the SNR by reasonably modifying the sensor design can reduce estimation uncertainties by 10% or more.

©2012 Optical Society of America

**OCIS codes:** (010.0280) Remote sensing and sensors; (010.4450) Oceanic optics; (110.4280) Noise in imaging systems.

---

## References and links

1. K. L. Carder, S. K. Hawes, K. A. Baker, R. C. Smith, R. G. Steward, and B. G. Mitchell, "Reflectance model for quantifying chlorophyll *a* in the presence of productivity degradation products," *J. Geophys. Res.* **96**(C11), 20599–20611 (1991).
2. F. E. Müller-Karger, J. J. Walsh, R. H. Evans, and M. B. Meyers, "On the seasonal phytoplankton concentration and sea surface temperature cycles of the Gulf of Mexico as determined by satellites," *J. Geophys. Res.* **96**(C7), 12645–12665 (1991).
3. K. L. Carder, F. R. Chen, Z. P. Lee, S. K. Hawes, and D. Kamikowski, "Semianalytic moderate-resolution imaging spectrometer algorithms for chlorophyll *a* and absorption with bio-optical domains based on nitrate-depletion temperatures," *J. Geophys. Res.* **104**(C3), 5403–5421 (1999).
4. C. Hu, K. L. Carder, and F. E. Müller-Karger, "Atmospheric correction of SeaWiFS imagery over turbid coastal waters: a practical method," *Remote Sens. Environ.* **74**(2), 195–206 (2000).
5. M. Babin, D. Stramski, G. M. Ferrari, H. Claustre, A. Bricaud, G. Obolensky, and N. Hoepffner, "Variations in the light absorption coefficients of phytoplankton, nonalgal particles, and dissolved organic matter in coastal waters around Europe," *J. Geophys. Res.* **108**, 3211 (2003), doi:10.1029/2001JC000882.
6. K. L. Carder, F. R. Chen, J. P. Cannizzaro, J. W. Campbell, and B. G. Mitchell, "Performance of the MODIS semi-analytical ocean color algorithm for chlorophyll-*a*," *Adv. Space Res.* **33**(7), 1152–1159 (2004).
7. M. Darecki and D. Stramski, "An evaluation of MODIS and SeaWiFS bio-optical algorithms in the Baltic Sea," *Remote Sens. Environ.* **89**(3), 326–350 (2004).
8. G. Dall'Olmo, A. A. Gitelson, D. C. Rundquist, B. Leavitt, T. Barrow, and J. C. Holz, "Assessing the potential of SeaWiFS and MODIS for estimating chlorophyll concentration in turbid productive waters using red and near-infrared bands," *Remote Sens. Environ.* **96**(2), 176–187 (2005).

Report Documentation Page			Form Approved OMB No. 0704-0188	
<p>Public reporting burden for the collection of information is estimated to average 1 hour per response, including the time for reviewing instructions, searching existing data sources, gathering and maintaining the data needed, and completing and reviewing the collection of information. Send comments regarding this burden estimate or any other aspect of this collection of information, including suggestions for reducing this burden, to Washington Headquarters Services, Directorate for Information Operations and Reports, 1215 Jefferson Davis Highway, Suite 1204, Arlington VA 22202-4302. Respondents should be aware that notwithstanding any other provision of law, no person shall be subject to a penalty for failing to comply with a collection of information if it does not display a currently valid OMB control number.</p>				
1. REPORT DATE <b>13 JAN 2012</b>	2. REPORT TYPE	3. DATES COVERED <b>00-00-2012 to 00-00-2012</b>		
<b>4. TITLE AND SUBTITLE</b> <b>Impact of signal-to-noise ratio in a hyperspectral sensor on the accuracy of biophysical parameter estimation in case II waters</b>			5a. CONTRACT NUMBER	
			5b. GRANT NUMBER	
			5c. PROGRAM ELEMENT NUMBER	
<b>6. AUTHOR(S)</b>			5d. PROJECT NUMBER	
			5e. TASK NUMBER	
			5f. WORK UNIT NUMBER	
<b>7. PERFORMING ORGANIZATION NAME(S) AND ADDRESS(ES)</b> <b>Naval Research Laboratory, Washington, DC, 20375</b>		8. PERFORMING ORGANIZATION REPORT NUMBER		
<b>9. SPONSORING/MONITORING AGENCY NAME(S) AND ADDRESS(ES)</b>			10. SPONSOR/MONITOR'S ACRONYM(S)	
			11. SPONSOR/MONITOR'S REPORT NUMBER(S)	
<b>12. DISTRIBUTION/AVAILABILITY STATEMENT</b> <b>Approved for public release; distribution unlimited</b>				
<b>13. SUPPLEMENTARY NOTES</b>				
<b>14. ABSTRACT</b> <p><b>Errors in the estimated constituent concentrations in optically complex waters due solely to sensor noise in a spaceborne hyperspectral sensor can be as high as 80%. The goal of this work is to elucidate the effect of signal-to-noise ratio (SNR) on the accuracy of retrieved constituent concentrations. Large variations in the magnitude and spectral shape of the reflectances from coastal waters complicate the impact of SNR on the accuracy of estimation. Due to the low reflectance of water, the actual SNR encountered for a water target is usually quite lower than the prescribed SNR. The low SNR can be a significant source of error in the estimated constituent concentrations. Simulated and measured at-surface reflectances were used in this study. A radiative transfer code, Tafkaa, was used to propagate the at-surface reflectances up and down through the atmosphere. A sensor noise model based on that of the spaceborne hyperspectral sensor HICO was applied to the at-sensor radiances. Concentrations of chlorophyll-a, colored dissolved organic matter, and total suspended solids were estimated using an optimized error minimization approach and a few semi-analytical algorithms. Improving the SNR by reasonably modifying the sensor design can reduce estimation uncertainties by 10% or more.</b></p>				
<b>15. SUBJECT TERMS</b>				
<b>16. SECURITY CLASSIFICATION OF:</b> a. REPORT      b. ABSTRACT      c. THIS PAGE <b>unclassified</b> <b>unclassified</b> <b>unclassified</b>			<b>17. LIMITATION OF ABSTRACT</b> <b>Same as Report (SAR)</b>	<b>18. NUMBER OF PAGES</b> <b>22</b>
				<b>19a. NAME OF RESPONSIBLE PERSON</b>

9. C. O. Davis, M. Kavanaugh, R. Letelier, P. W. Bissett, and D. Kohler, "Spatial and spectral resolution considerations for imaging coastal waters," Proc. SPIE, Characterization and Variability of the Coastal Ocean: Composition and Bio-optical Properties II **6680**, 66800P, doi:10.1117/12.734288 (2007).
10. G. Chang, K. Mahoney, A. Briggs-Whitmire, D. D. R. Kohler, C. D. Mobley, M. Lewis, M. A. Moline, E. Boss, M. Kim, W. Philpot, and T. D. Dickey, "The new age of hyperspectral oceanography," *Oceanography* (Wash. D.C.) **17**(2), 16–23 (2004).
11. M. Sydor, R. W. Gould, R. A. Arnone, V. I. Haltrin, and W. Goode, "Uniqueness in remote sensing of the inherent optical properties of ocean water," *Appl. Opt.* **43**(10), 2156–2162 (2004).
12. P. W. Bissett, R. A. Arnone, C. O. Davis, T. D. Dickey, D. Dye, D. D. R. Kohler, and R. W. Gould, "From meters to kilometers - a look at ocean color scales of variability, spatial coherence, and the need for fine scale remote sensing in coastal ocean optics," *Oceanography* (Wash. D.C.) **17**(2), 32–43 (2004).
13. W. J. Moses, A. A. Gitelson, S. Berdnikov, and V. Povazhnyy, "Estimation of chlorophyll-*a* concentration in case II waters using MODIS and MERIS data - successes and challenges," *Environ. Res. Lett.* **4**(045005), 8 (2009).
14. A. Morel, "In-water and remote measurement of ocean color," *Boundary-Layer Meteorol.* **18**(2), 177–201 (1980).
15. IOCCG, "Remote sensing of ocean colour in coastal, and other optically-complex, waters," S. Sathyendranath, ed., Reports of the International Ocean-Colour Coordinating Group, No. 3, IOCCG, Dartmouth, Canada (2000).
16. V. E. Brando and A. G. Dekker, "Satellite hyperspectral remote sensing for estimating estuarine and coastal water quality," *IEEE Trans. Geosci. Rem. Sens.* **41**(6), 1378–1387 (2003).
17. J. H. Bowles, S. J. Maness, W. Chen, C. O. Davis, T. F. Donato, D. B. Gillis, D. Korwan, G. Lamela, M. J. Montes, W. J. Rhea, and W. A. Snyder, "Hyperspectral imaging of an inter-coastal waterway," Proc. SPIE, Monitoring and Change Detection **5983**, 59830F, doi:10.1117/12.627676 (2005).
18. R. P. Stumpf and P. J. Werdell, "Adjustment of ocean color sensor calibration through multi-band statistics," *Opt. Express* **18**(2), 401–412 (2010).
19. A. Morel and L. Prieur, "Analysis of variations in ocean color," *Limnol. Oceanogr.* **22**(4), 709–722 (1977).
20. A. Eckardt, S. Hofer, C. Neumann, and W. Skrbek, "SNR estimation for advanced hyperspectral space instrument," Proc. SPIE, IR Instruments **5883**, 588303, doi:10.1117/12.609236 (2005).
21. M. Defoin-Platel and M. Chami, "How ambiguous is the inverse problem of ocean color in coastal waters?" *J. Geophys. Res.* **112**(C3), C03004 (2007), doi:10.1029/2006JC003847.
22. J. M. Duarte, M. Velez-Reyes, S. Tarantola, F. Gilbes, and R. Armstrong, "A probabilistic sensitivity analysis of water-leaving radiance to water constituents in coastal shallow waters," Proc. SPIE, Ocean-color Remote Sensing: Inherent Optical Properties and Applications I **5155**, 162–173 (2003).
23. M. S. Salama and A. Stein, "Error decomposition and estimation of inherent optical properties," *Appl. Opt.* **48**(26), 4947–4962 (2009).
24. Z. P. Lee, R. Arnone, C. Hu, P. J. Werdell, and B. Lubac, "Uncertainties of optical parameters and their propagations in an analytical ocean color inversion algorithm," *Appl. Opt.* **49**(3), 369–381 (2010).
25. D. R. Korwan, R. L. Lucke, M. Corson, J. H. Bowles, B. C. Gao, R. R. Li, M. J. Montes, W. A. Snyder, N. R. McGlothlin, S. D. Butcher, D. L. Wood, C. O. Davis, and W. D. Miller, "The hyperspectral imager for the coastal ocean (HICO) – design and early results," in IGRSS Workshop on Hyperspectral Image and Signal Processing: Evolution in Remote Sensing (IEEE, 2010), 14–16 June 2010, pp. 1–4, doi: 10.1109/WHISPERS.2010.5594935.
26. R. L. Lucke, M. Corson, N. R. McGlothlin, S. D. Butcher, D. L. Wood, D. R. Korwan, R. R. Li, W. A. Snyder, C. O. Davis, and D. T. Chen, "Hyperspectral Imager for the Coastal Ocean: instrument description and first images," *Appl. Opt.* **50**(11), 1501–1516 (2011).
27. J. R. Schott, *Remote Sensing: The Image Chain Approach*, 2nd ed. (Oxford University Press Inc., New York, 2007), p. 666.
28. R. L. Lucke and R. A. Kessel, "Signal-to-noise ratio, contrast-to-noise ratio and exposure time for imaging systems with photon-limited noise," *Opt. Eng.* **45**(5), 056403 (2006).
29. C. D. Mobley, "A numerical model for the computation of radiance distributions in natural waters with wind roughened surfaces," *Limnol. Oceanogr.* **34**(8), 1473–1483 (1989).
30. C. D. Mobley, *Light and Water: Radiative Transfer in Natural Waters* (Academic Press Inc., San Diego, California, 1994), p. 592.
31. C. D. Mobley and L. K. Sundman, *Hydrolight 5 Ecolight 5 Technical Documentation*, 1st ed., (Sequoia Scientific Inc., Bellevue, WA, 2008).
32. A. Gitelson, D. Gurlin, W. Moses, and T. Barrow, "A bio-optical algorithm for the remote estimation of the chlorophyll-*a* concentration in case 2 waters," *Environ. Res. Lett.* **4**(045003), 5 (2009).
33. W. J. Moses, "Satellite-based estimation of chlorophyll-*a* concentration in turbid productive waters," PhD dissertation, University of Nebraska-Lincoln, Lincoln, NE (2009).
34. A. Gitelson, D. Gurlin, W. Moses, and Y. Yacobi, "Remote estimation of chlorophyll-*a* concentration in inland, estuarine, and coastal waters," pp. 449–478, in *Advances in Environmental Remote Sensing: Sensors, Algorithms, and Applications*, Q. Weng, ed., (Taylor and Francis Group, Boca Raton, Florida), 610 p. (2011).
35. D. Gurlin, A. A. Gitelson, and W. J. Moses, "Remote estimation of chl-*a* concentration in turbid productive waters – return to a simple two-band NIR-red model?" *Remote Sens. Environ.* **115**(12), 3479–3490 (2011).
36. B. C. Gao, M. J. Montes, Z. Ahmad, and C. O. Davis, "Atmospheric correction algorithm for hyperspectral remote sensing of ocean color from space," *Appl. Opt.* **39**(6), 887–896 (2000).

37. M. J. Montes, B. C. Gao, and C. O. Davis, "A new algorithm for atmospheric correction of hyperspectral remote sensing data," Proc. SPIE, Geo-spatial Image and Data Exploitation II, W. E. Roper, ed., **4383**, 23–30 (2001).
38. F. A. Kruse, J. W. Boardman, and J. F. Huntington, "Comparison of EO-1 Hyperion and airborne hyperspectral remote sensing data for geologic applications," in *Proceedings of IEEE Aerospace Conference* **3**, 3–1501 – 3–1513, doi: 10.1109/AERO.2002.1035288 (2002).
39. F. A. Kruse, J. W. Boardman, and J. F. Huntington, "Comparison of airborne hyperspectral data and eo-1 hyperion for mineral mapping," *IEEE Trans. Geosci. Rem. Sens.* **41**(6), 1388–1400 (2003).
40. C. B. Markwardt, "Non-Linear Least Squares Fitting in IDL with MPFIT," in *Proceedings of the Astronomical Data Analysis Software and Systems XVIII*, ASP Conference Series, D. Bohlander, D. Durand, and P. Dowler, eds., **411**, 251–254 (2009).
41. J. J. Moré, "The Levenberg-Marquardt algorithm: implementation and theory," in *Numerical analysis*, G. Watson, ed., **630**, 105–116, doi: 10.1007/BFb0067700 (1978).
42. J. J. Moré and S. J. Wright, *Optimization Software Guide*, vol. 14, (SIAM Publications, 1993).
43. K. Levenberg, "A method for the solution of certain non-linear problems in least squares," *Q. Appl. Math.* **2**, 164–168 (1944).
44. D. W. Marquardt, "An algorithm for least-squares estimation of nonlinear parameters," *SIAM J. Appl. Math.* **11**(2), 431–441 (1963).
45. J. E. O'Reilly, S. Maritorena, B. G. Mitchell, D. A. Siegel, K. L. Carder, S. A. Garver, M. Kahru, and C. McClain, "Ocean color chlorophyll algorithms for SeaWiFS," *J. Geophys. Res.- Oceans* **103**(C11), 24937–24953 (1998).
46. J. E. O'Reilly, "SeaWiFS postlaunch calibration and validation analyses, part 3," NASA Tech. Memo. 2000–206892, Vol. 11, 49 pp., S. B. Hooker and E. R. Firestone, eds., NASA Goddard Space Flight Center, MD (2000).
47. A. Gitelson, "The peak near 700 nm on radiance spectra of algae and water - relationships of its magnitude and position with chlorophyll concentration," *Int. J. Remote Sens.* **13**(17), 3367–3373 (1992).
48. A. Gitelson, G. Dall'Olmo, W. Moses, D. C. Rundquist, T. Barrow, T. R. Fisher, D. Gurlin, and J. Holz, "A simple semi-analytical model for remote estimation of chlorophyll-a in turbid waters: validation," *Remote Sens. Environ.* **112**(9), 3582–3593 (2008).
49. W. Moses, A. Gitelson, S. Berdnikov, and V. Povazhnyy, "Satellite estimation of chlorophyll-a concentration using the red and NIR bands of MERIS - the Azov Sea case study," *IEEE Geosci. Remote Sens. Lett.* **6**(4), 845–849 (2009).
50. G. Dall'Olmo and A. A. Gitelson, "Effect of bio-optical parameter variability on the remote estimation of chlorophyll-a concentration in turbid productive waters: experimental results," *Appl. Opt.* **44**(3), 412–422 (2005).
51. I. M. Levin and E. Levina, "Effect of atmospheric interference and sensor noise in retrieval of optically active materials in the ocean by hyperspectral remote sensing," *Appl. Opt.* **46**(28), 6896–6906 (2007).

## 1. Introduction

As natural habitats for a wide variety of aquatic flora and fauna, estuarine and coastal waters play crucial roles in maintaining global biodiversity. However, these complex ecosystems have been under tremendous ecological stress in recent years due to natural as well as anthropogenic factors, and thus it is imperative to develop robust methods that can be used to regularly monitor the biophysical conditions of these waters. The trophic and biophysical status of these waters are usually determined by estimating the concentrations of optically active materials in water, such as, total suspended solids (TSS), colored dissolved organic matter (CDOM), and chlorophyll-*a* (chl-*a*). In addition to the environmental cause, there are also commercial, recreational, and military interests to characterizing and monitoring estuarine and coastal systems. Characterizing the bottom type and depth is crucial for many purposes, such as, seafood safety, maritime navigation, underwater geologic studies, global climate studies, habitat management, recreational management, coastal erosion control, etc.

In the last several decades, airborne and spaceborne remote sensing have proven to be very effective and successful tools for monitoring water bodies, particularly the open ocean waters. However, monitoring coastal waters has been more complicated and challenging than monitoring open ocean waters (Case I) because of the inherent optical complexity of the Case II coastal waters [1–8] and also the fact that coastal waters are spatially and temporally more dynamic [9] than open ocean waters. Commonly used spaceborne multispectral ocean color sensors such as SeaWiFS (Sea-viewing Wild Field-of-view Sensor), MODIS (MODerate resolution Imaging Spectroradiometer), and MERIS (MEdium Resolution Imaging

Spectrometer) do not have the necessary spectral [10, 11] and spatial resolution [12, 13] for detailed coastal analysis from a biophysical standpoint.

Advances in instrumentation technologies and data processing capabilities [10] have facilitated the development and operational use of hyperspectral sensors with numerous contiguous narrow spectral bands and high spatial resolution. Hyperspectral sensors are capable of measuring the necessary spectral and spatial information from the optically complex and highly dynamic coastal waters. Numerous studies have been conducted using airborne hyperspectral sensors on different coastal regions around the world. Airborne remote sensing offers the advantage of increased control over the data collection process. The spatial resolution can be adjusted by flying the sensor at different altitudes or changing the focal length of the sensor. At typical aircraft altitudes (less than, say, 15,000 ft) the intervening atmosphere is significantly less than what would be encountered from the altitude of a typical spaceborne platform. However, each data collection expedition is a costly endeavor and the results and inferences are usually confined to the specific region and environment in which the data were collected, which hinders the development of universal algorithms that can be routinely applied to coastal waters around the globe. Efforts have been made in recent years to launch spaceborne hyperspectral sensors. NASA (National Aeronautics and Space Administration) launched the first spaceborne hyperspectral sensor, Hyperion, in 2000. Several other spaceborne hyperspectral sensors have been launched recently. The European Space Agency's CHRIS (Compact High Resolution Imaging Spectrometer) was launched in 2001. The Air Force Research Laboratory's ARTEMIS (Advanced Responsive Tactically Effective Military Imaging Spectrometer) was launched in 2009. The Naval Research Laboratory launched HICO (Hyperspectral Imager for the Coastal Ocean) in 2009. The German Aerospace Center (Deutsches Zentrum für Luft- und Raumfahrt; DLR) is spearheading the development of EnMAP (Environmental Mapping and Analysis Program), which is scheduled to be launched in 2013.

The advantage gained from the fine spectral information obtained from hyperspectral sensors can be offset by the lower signal-to-noise ratio (SNR) when compared to multispectral sensors because of the fewer number of photons captured by each detector due to the narrower width of the spectral channels. The photon noise has a significant impact on the retrieved reflectances, and therefore, the estimated biophysical parameters. This is especially the case for data acquired over water, which is highly absorptive and whose radiometric contribution to the at-sensor radiance peaks at only about 15% or less of the total radiance received by the sensor [14–18]. Because of this low signal level and large atmospheric contribution, instrument design is of particular importance for sensors intended for acquiring data over water. The larger magnitude of signal from the land makes systems designed for land work less dependent on sensor responsiveness.

The SNR of a sensor is often specified as a single number that is the maximum value calculated based on a standard target. For sensors that operate over water, a spectrally uniform 5% albedo is commonly used as the standard. However, the reflectivity of water is often lower than 5%, especially in the near infrared (NIR) region, and the optical complexity of Case II waters produces a complex reflectance pattern [19] that is not spectrally uniform. Thus the actual SNR encountered for optically complex water targets is usually lower than the prescribed SNR and is very much dependent on the magnitude and spectral shape of the radiance received at the sensor [20].

Past analyses using multispectral approaches have revealed that the task of retrieving inherent optical properties from remote sensing reflectance to derive geophysical and biophysical products is an ill-posed problem because of the non-uniqueness of the optical properties (e.g [21]). In other words, the same reflectance values can be obtained for more than one set of optical properties of the constituents in water [11, 22, 23]. Besides, there are other sources of error such as those arising from the calibration of the sensor and the procedure to correct for the atmospheric interference on the measured reflectance, in addition

to errors due to photon noise in the sensor. In order to correctly assess the performance of reflectance-based algorithms, it is necessary to have a quantitative understanding of the various sources of error [23, 24].

In this study, we have investigated the effect of a sensor's photon noise on the accuracy of retrievals of the concentrations of chl-*a*, CDOM, and TSS in coastal waters using a spaceborne hyperspectral sensor. By adjusting several components of the sensor configuration, we obtained different magnitudes and spectral shapes of SNR. These variations in SNR affect the performance of spectral algorithms depending on the spectral regions in which the algorithms operate. The objectives were to assess the spectral effects of variations in SNR, arrive at quantitative estimates of expected errors due to noise in the retrievals of the concentrations of chl-*a*, CDOM, and TSS in typical coastal waters for a spaceborne sensor, and make feasible recommendations for sensor configurations that would result in the most accurate estimates of optically active material in coastal waters, judging purely on the basis of the effects of photon noise.

We have used a model developed for HICO as the basis for the sensor model in this study. Here we consider the noise to be composed of the photon noise (shot noise), the dark noise, the readout noise, and the digitization noise. It must be noted that we have not considered systematic errors due to factors such as fixed pattern noise, absolute radiometric uncertainty, image distortions, stray light, etc., and as such, the retrieval accuracies reported herein represent a lower bound on what would be the real-life results. The effective SNR changes due to variations in magnitudes and spectral shapes of the retrieved reflectance, which varies as the constituent concentrations change and as the noise changes depending on the sensor configuration. The impact of these variations on the accuracy of the retrieved constituent concentrations is the primary topic explored in this paper. The effects of atmospheric contribution and their impact on the accuracy of the retrieval of constituent concentrations are important and could potentially be higher than the effects of sensor noise. However, an analysis of the atmospheric effects is not included in this study, which considers only the effects of sensor noise that is inevitably present regardless of the magnitudes of other sources of errors such as those mentioned above. Thus this study presents a lower bound of retrieval errors that can be expected in a real scenario where the aforementioned sources of errors will further affect the retrieval accuracy.

The remainder of the paper is laid out as follows: We first describe the sensor model of HICO. We then describe our approach, which involved the following steps, (i) generation/measurement of at-surface remote sensing reflectance (Rrs) spectra, (ii) propagation of the at-surface Rrs through the atmosphere to estimate at-sensor radiance, (iii) addition of noise to the at-sensor radiance, (iv) atmospheric correction of the at-sensor radiance to retrieve the at-surface Rrs, and (v) retrieval of constituent concentrations from the atmospherically corrected at-surface Rrs. The analysis is presented in the 'Results and discussions' section, followed by concluding remarks.

## 2. Materials and methods

### 2.1. HICO noise model

HICO is the first spaceborne hyperspectral sensor designed specifically for studying the coastal systems [25, 26]. It was launched on 11 September 2009 and docked on to the International Space Station, and has been fully operational since 01 October 2009. The sensor is a conventional hyperspectral imaging sensor with an Offner grating-type spectrometer and operates in pushbroom mode. The camera has a  $512 \times 512$  CCD array with  $16 \mu\text{m}$  wide detector pixels. The sensor operates in the spectral range,  $350 - 1080$  nm, with a spectral resolution of  $5.73$  nm. From a nadir viewing angle, its cross-track and along-track ground coverage are  $42$  km and  $192$  km, respectively, yielding a total scene area of approximately

8000 km<sup>2</sup>. The ground sampling distance is about 90 m at nadir. Complete information on the characteristics of the sensor has been reported by Lucke et al [26].

The total noise in the sensor is the sum of the photon noise (shot noise), the dark noise, the readout noise, and the digitization noise.

The photon noise arises due to variations in the number of photons that are detected by the sensor per unit time. The number of photons detected per unit time follows a Poisson distribution whose standard deviation is the square root of the total number of detected photons. Thus the photon noise in the sensor is the square root of the total signal (electrons) generated by the photons striking the sensor. The total signal generated at the sensor is given by [27, 28],

$$\text{Signal} = \frac{\lambda}{hc} L_{\Delta\lambda} \frac{\pi}{4} \frac{D^2}{f^2} p^2 T \eta_{\text{sys}}, \quad (1)$$

where,

$\lambda$  is the wavelength of the incident radiation (in units of  $\mu\text{m}$ )

$h$  is the planck's constant

$c$  is the velocity of electromagnetic radiation (in units of  $\text{m s}^{-1}$ )

$L_{\Delta\lambda}$  is the incoming radiance at the sensor in the waveband  $\Delta\lambda$  (in units of  $\text{W m}^{-2} \mu\text{m}^{-1} \text{Sr}^{-1}$ )

$D$  is the diameter of the aperture (in units of m)

$f$  is the focal length of the imaging system (in units of m)

$p$  is the spatial width of the detector pixel (in units of m)

$T$  is the exposure time (in units of s)

$\eta_{\text{sys}}$  is the overall system efficiency, which is given by,

$\eta_{\text{sys}} = \eta_{\text{op}} \times \eta_{\text{QE}} \times \eta_g$ , where,

$\eta_{\text{op}}$  is the optical transmissive efficiency of the system

$\eta_{\text{QE}}$  is the quantum efficiency of the detector

$\eta_g$  is the grating efficiency, which is given by,

$$\eta_g(\lambda) = \eta_{g0} \text{sinc}^2 \left[ f_g \left( 1 - \frac{\lambda_b}{\lambda} \right) \right], \text{ where,}$$

$\eta_{g0}$  is the grating efficiency at the blaze wavelength,  $\lambda_b$ ,

$$\text{sinc } cx = (\sin \pi x) / \pi x$$

$f_g$  is the fraction of a grating groove that is at the blaze angle.

$$\text{Thus the photon noise} = \sqrt{\frac{\lambda}{hc} L_{\Delta\lambda} \frac{\pi}{4} \frac{D^2}{f^2} p^2 T \eta_{\text{sys}}} \quad (2)$$

$h$  ( $= 6.63 \times 10^{-34}$  Js $^{-1}$ ) and  $c$  ( $= 3 \times 10^8$  ms $^{-1}$ ) are constants. Nominal values for the relevant instrument-related quantities in Eq. (1) were taken from the corresponding values for HICO. The focal length,  $f$ , of the imaging system is 0.067 m and the diameter of the aperture,  $D$ , is 0.019 m, for an  $f$ -number ( $= f/D$ ) of 3.5. The spatial width of the detector pixel,  $p$ , is  $16 \times 10^{-6}$  m. The exposure time,  $T$ , is calculated as

$$T = GMC \times \frac{GSD}{V}, \text{ where } GMC \text{ is the ground motion compensation factor, } GSD \text{ is the}$$

ground sampling distance, and  $V$  is the ground velocity of the satellite, calculated as,

$$V = \frac{r_E^2}{(r_E + H_s)} \sqrt{\frac{g}{(r_E + H_s)}}, \text{ where } r_E \text{ is the radius of the Earth, } H_s \text{ is the altitude of the}$$

satellite above the Earth's surface, and  $g$  is the Earth's gravitational acceleration ( $\approx 9.8$  m s $^{-2}$ ).  $GMC$  refers to the possibility of controlling a sensor's line of sight (LOS) during an observation to increase the exposure time for a point on the ground.  $GMC = 1$  for HICO, i.e.,  $GMC$  is not used and the LOS is swept across the ground by the orbital motion of the ISS.

Usually, the only part of system efficiency that is a free parameter for the instrument designer is the blaze wavelength of the grating. For HICO, the blaze wavelength of the grating,  $\lambda_b$ , is set as 400 nm and the groove fraction,  $f_g$ , as 0.92.

The standard deviation of a dark image acquired by HICO was taken to represent the dark noise as well as the readout noise and the digitization noise. Thus the total noise was calculated as

$$\text{Noise} = \sqrt{(\text{Shot Noise})^2 + (\text{Dark Noise})^2 + (\text{Readout Noise})^2 + (\text{Digitization Noise})^2} \quad (3)$$

For HICO, the sum of the last three terms in the square root, measured in electrons, is about  $100^2$ , that is, the noise contribution from these terms is the same as the shot noise contributed by  $10^4$  electrons, so we may conclude that when the signal exceeds  $10^4$  electrons, the data are essentially shot-noise-limited. For HICO, the relation between the number of electrons,  $N_e$ , and digital numbers,  $DN$ , from the sensor is  $DN \approx N_e/26$  [26]. Thus for  $DN > 400$ , the data are considered shot-noise-limited.

$$\text{The signal-to-noise ratio is, } \text{SNR} = \frac{\text{Incoming signal}}{\text{Noise}} \quad (4)$$

Even though the HICO sensor model was used as the basis for the SNR calculations in this study, the inferences made herein are not necessarily tied to HICO but are general, with a broad application to spaceborne sensors with similar SNR values.

## 2.2. SNR variations with sensor configuration

The SNR varies depending on the sensor configuration. Sensor design involves a series of tradeoffs between instrument cost and performance, with the objective being achieving the best performance within the cost constraints. Within these tradeoffs, there are parameters that can be changed in ways that may impact requirements placed on the foreoptics, the spectrograph, or the focal plane. The most obvious of these parameters are the blaze wavelength and the diameter of the aperture. The change in blaze wavelength can be considered a nearly cost-free adjustment. However, increasing the aperture size to improve the SNR imposes a series of additional costs. These costs can be simple or complicated depending on the need to make changes in the spectrometer to accommodate the larger foreoptic. The aperture size is increased by decreasing the F-number.

We investigated the variations in SNR as the sensor configuration is changed and the impact of these variations on the accuracy of the estimated constituent concentrations.

## 2.3. Data processing

### 2.3.1. At-surface reflectance spectra

The data used in this study consisted of two sets of remote sensing reflectances (Rrs) at the water surface: (i) reflectances that were synthetically generated using the radiative transfer model Ecolight [29–31] and (ii) reflectances that were actually measured using field spectrometers in turbid productive lakes in Nebraska, USA. The steps of the data processing are illustrated in Fig. 1.

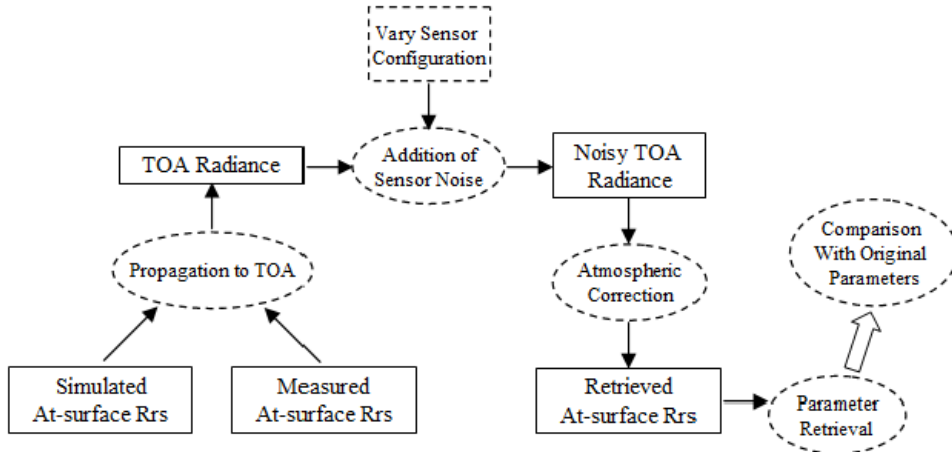


Fig. 1. Flow chart of the data processing steps (TOA: top of atmosphere)

#### 1. Synthetically generated at-surface reflectance spectra

Ecolight simulations were executed for low, medium, and high concentrations of chl-*a*, TSS, and CDOM, typically encountered in coastal waters (Table 1). Combining different levels of constituent concentrations, 49 reflectance spectra were generated (Fig. 2). The water was assumed to be optically deep, which is true for turbid productive waters. All other relevant parameters (such as, sediment type, phase function of the chl-*a* and sediment particles, etc.) for the Ecolight simulations were kept the same for all 49 spectra. The Rrs spectra were simulated at the central wavelength locations of HICO. Only data within the spectral range of 400 – 800 nm was used in the analysis. Figures with data beyond this spectral range are shown for illustrative purpose only.

#### 2. In situ measured at-surface reflectance spectra

*In situ* measured reflectances were taken from data collected in turbid productive lakes in Nebraska, USA [32–35]. Twenty seven reflectance spectra that spanned a wide range of concentrations of chl-*a*, TSS, and CDOM were chosen. The descriptive statistics of the corresponding constituent concentrations are given in Table 2. Complete description of the *in situ* data set can be found in Gitelson et al. (2009, 2011), Gurlin et al. (2011), and Moses (2009) [32–35].

**Table 1. Ranges of concentrations of chl-*a* and TSS, and absorption of CDOM at 440 nm, for which reflectance spectra were generated using Ecolight.**

	Chl- <i>a</i> ( $\text{mg m}^{-3}$ )	TSS ( $\text{g m}^{-3}$ )	$\alpha_{\text{CDOM}}(440)$ ( $\text{m}^{-1}$ )
Low	2	1	0.1
Medium	15, 25	4, 8	1
High	50	14, 20	2

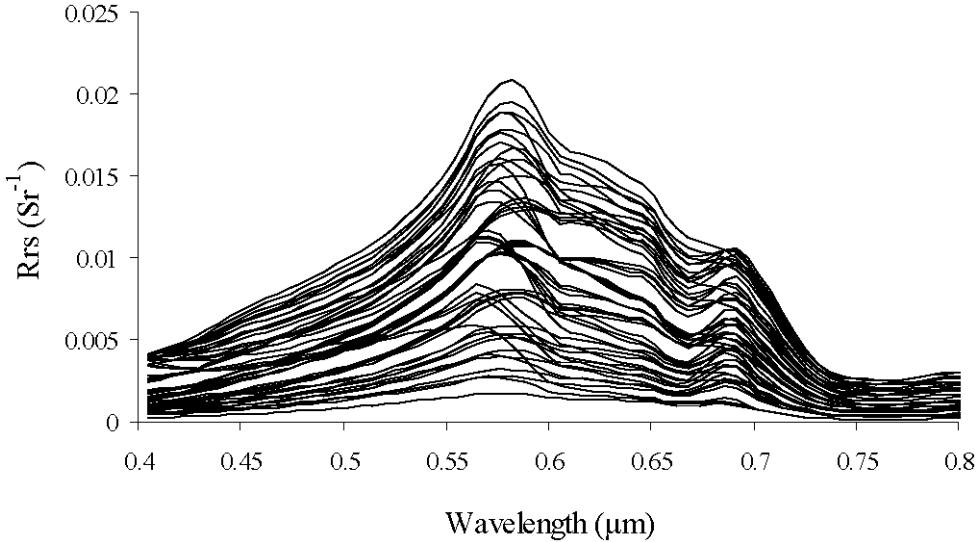


Fig. 2. Reflectance spectra simulated using Ecolight.

**Table 2. Descriptive statistics of the constituent concentrations in the *in situ* measured data set.  $\alpha_{CDOM}(440)$  is the absorption coefficient of CDOM at 440 nm. Coefficient of variation is the ratio of the standard deviation to the mean.**

Parameter	Min	Max	Median	Mean	Standard Deviation	Coefficient of Variation
Chl- $a$ ( $\text{mg m}^{-3}$ )	2.27	80.16	28.59	33.33	24.052	0.722
TSS ( $\text{g m}^{-3}$ )	1.19	15.00	8.89	7.86	3.717	0.473
$\alpha_{CDOM}(440)$ ( $\text{m}^{-1}$ )	0.46	1.45	0.90	0.90	0.251	0.278

### 2.3.2. Propagation to top-of-atmosphere (TOA) radiance

A forward version of the atmospheric correction radiative transfer model, Tafkaa [36, 37], was used to simulate the atmospheric effects and propagate the at-surface Rrs (synthetically generated as well as measured *in situ*) through the atmosphere in order to derive the incoming radiance at the sensor. The at-sensor radiances were generated at HICO wavelengths. The total radiance at the sensor is given by,

$$L_t = L_p + L_{sfc}t + \frac{\rho_w \mu_o E_o t'}{\pi} \quad (5)$$

where,

$L_t$  is the radiance received at the sensor

$L_p$  is the atmospheric path radiance

$L_{sfc}$  is the specularly reflected radiance from the water surface

$t$  is the transmittance of  $L_{sfc}$  through the atmosphere

$\rho_w$  is the remote sensing reflectance of water

$\mu_o$  ( $= \cos \theta_o$ ) is the cosine of the solar zenith angle ( $\theta_o$ )

$E_o$  is the solar irradiance at the top of the atmosphere

$t'$  is the transmittance of the radiance from water through the atmosphere.

Solar illumination conditions at the sensor, as specified by the date and time of data acquisition, the geographic location of the target, the ground elevation, the sensor altitude, and the viewing angles of the sensor in the zenith and azimuth directions, were kept the same for all at-surface Rrs spectra. The location of the target and the date/time used in the simulation corresponded to a solar zenith angle of 58 degrees. The effective SNR varies with the solar zenith angle and increases at low solar zenith angles [38, 39]. Atmospheric parameters, such as, the atmospheric model, the types of atmospheric gases, the ozone amount, the column water vapor amount, the relative humidity, the aerosol model, the aerosol optical depth at 550 nm, and the wind speed, were also kept the same (Table 3).

**Table 3. Geographic, illumination, and atmospheric parameter values used for the upward propagation of the at-surface Rrs.**

Parameter	Value
Date	09 Feb 2011
Time	15 hrs 30 min (GMT)
Latitude	37°30'
Longitude	-76°10'
Ground Elevation	0 km
Sensor Altitude	400 km
Sensor Zenith Angle	0°
Sensor Azimuth Angle	0°
Atmospheric Model	Mid-Latitude Summer
Atmospheric Gases	H <sub>2</sub> O, CO <sub>2</sub> , O <sub>2</sub> , N <sub>2</sub> O, CO, CH <sub>4</sub> , O <sub>3</sub>
Ozone Amount	0.34 atm-cm
Column Water Vapor	2.50 cm
Relative Humidity	50%
Aerosol Model	Maritime
Aerosol Optical Depth at 550 nm	0.225581
Wind Speed	2 m s <sup>-1</sup>

### 2.3.3. Addition of noise

The noise was assumed to be normally distributed with a mean of zero and a standard deviation equal to the expected noise level. For example, for a radiance of 30 W m<sup>-2</sup> μm<sup>-1</sup> Sr<sup>-1</sup> and a SNR of 100, the standard deviation would be 0.3. Each of the incoming TOA radiance spectra was replicated to create a 1000-pixel image, with the random noise added to each of the 1000 spectra. Thus, noise-added at-sensor radiance images, each containing 1000 pixels, were produced for each of the original at-surface Rrs spectra. The SNR was also calculated for each Rrs spectrum. As can be seen (Fig. 3), SNR varies, especially in the green and red spectral regions, as the reflectance varies spectrally depending on the bio-optical properties of the water.

The effects of noise appear small on the at-sensor radiance (Fig. 4). However, when the contributions from the atmospheric path radiance and the specularly reflected radiance from the water surface, which form a significant portion of the at-sensor radiance (Fig. 4), are removed, the actual SNR is quite low and the impact of noise on incoming signal from the water target becomes quite significant. This fact is often obscured by the misleading high value of the prescribed SNR but is evident in the at-surface Rrs retrieved after atmospheric correction. As an example, the coefficient of variation (= standard deviation/mean) of the 1000 noisy atmospherically corrected at-surface Rrs and the plus/minus one standard deviation curves are shown in Fig. 5 for an original Rrs spectrum corresponding to chl-*a* = 2 mg m<sup>-3</sup>, *a*<sub>CDOM(440)</sub> = 0.1 m<sup>-1</sup>, and TSS = 1 g m<sup>-3</sup>. The variations in the reflectance due to low SNR are significant, especially in the blue, red, and NIR regions.

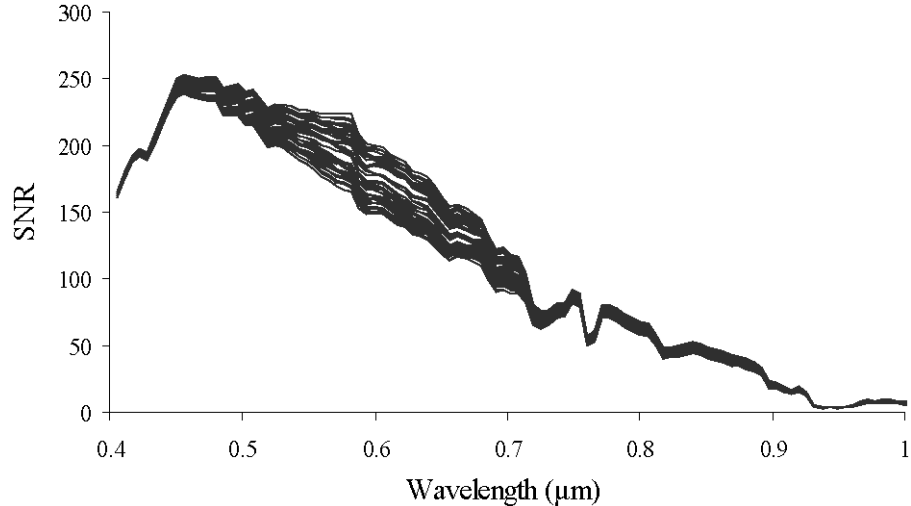


Fig. 3. At-sensor SNR curves for the synthetically generated Rrs spectra based on nominal HICO sensor configuration (see section 2.1).

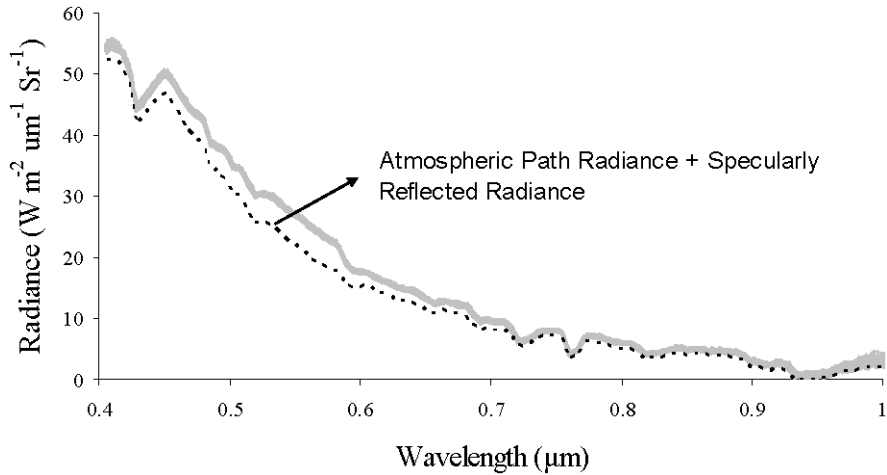


Fig. 4. Noise-added at-sensor radiance for water with  $\text{chl-}a = 2 \text{ mg m}^{-3}$ , TSS =  $1 \text{ g m}^{-3}$ , and  $a_{\text{CDOM}}(440) = 0.1 \text{ m}^{-1}$ . The dashed line represents the contribution from atmospheric path radiance and specularly reflected radiance from the water surface.

#### 2.3.4. Atmospheric correction

Tafkaa was used to remove the atmospheric effects from the noise-added at-sensor radiance and retrieve the at-surface reflectance (Fig. 5). The same illumination conditions and atmospheric parameters used for the upward propagation of the original at-surface Rrs spectra were used in the atmospheric correction process, thereby ensuring a complete removal of atmospheric effects.

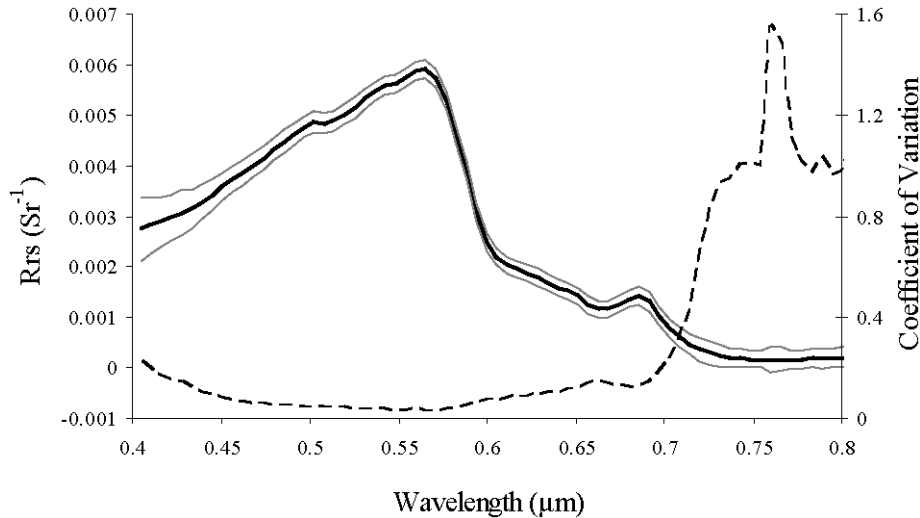


Fig. 5. Atmospherically corrected Rrs spectra for water with  $\text{chl-}a = 2 \text{ mg m}^{-3}$ , TSS =  $1 \text{ g m}^{-3}$ , and  $a_{\text{CDOM}}(440) = 0.1 \text{ m}^{-1}$ . The black curve represents the original at-surface Rrs spectrum. The gray curves represent mean plus/minus one standard deviation of the atmospherically corrected Rrs, and the dotted curve represents the coefficient of variation (on the secondary y-axis) of the retrieved at-surface Rrs after atmospheric correction following the addition of noise to the at-sensor radiance.

### 2.3.5. Estimation of constituent concentrations

An optimized error minimization approach and several semi-analytical algorithms were used to estimate the constituent concentrations from the atmospherically corrected noise-added at-surface Rrs spectra and compare the estimates to the original values. The optimized error minimization approach was used to estimate constituent concentrations from the noisy images produced from the at-surface Rrs spectra that were generated using Ecolight. The semi-analytical algorithms were used for noisy images from the Rrs spectra that were actually measured *in situ*.

#### 1. Optimized error minimization approach

The optimized error minimization approach was based on the idea of using a forward model (Ecolight) that relates Rrs to constituent concentrations (parameters of the model) and estimating the constituent concentrations by iteratively minimizing the squared difference between the modeled reflectances and the true reflectances. The parameter estimation was accomplished using MPFIT [40], which is a non-linear least squares curve fitting procedure. MPFIT is an enhancement of the FORTRAN-based software, MINPACK [41, 42], and was written for use with IDL (Interactive Data Language). The procedure basically fits a user-supplied model to a user-supplied set of data by iteratively estimating new values of model parameters that minimize the squared difference between the data and the model estimates. MPFIT uses the Levenberg-Marquardt [43, 44] method to iteratively minimize the squared difference. MPFIT requires initial estimates of parameter values and solves the problem by linearizing it around the set of parameter values at each iteration [40]. One of the advantages of MPFIT is that it allows placing constraints on the parameters.

Concentrations of chl-*a* and TSS, and the absorption of CDOM at 400 nm, were estimated for each of the 1000 pixels in the noise-added atmospherically corrected image for every original at-surface Rrs spectrum. For the MPFIT run with the Ecolight model, each noisy Rrs spectrum was considered as the true reflectance, with three varying parameters, namely, chl-*a* concentration, TSS concentration, and  $a_{\text{CDOM}}_{440}$ . The initial parameter values were the original constituent concentrations (see Table 1) that were used to generate the at-surface Rrs

spectrum from which the noisy image was generated. MPFIT generated optimal estimates of the constituent concentrations by iteratively minimizing the squared difference between the noisy spectrum and the spectrum generated (iteratively) by Ecolight for the given set of parameter values.

This kind of approach is suitable for hyperspectral data as it takes the whole spectral range, in this case 400–800 nm, into consideration and is therefore not extremely sensitive to noise at a particular spectral region and virtually gives the effect of averaging the effects of noise in the whole spectral range.

## 2. Semi-analytical algorithms

Some well established semi-analytical two-band and three-band algorithms, which rely on reflectances in two or three specific spectral bands for estimating constituent concentrations, were also used. Only chl-*a* concentration was estimated using these algorithms because algorithms such as these are not operational as yet for quantitatively estimating the concentrations of TSS and CDOM.

The following semi-analytical algorithms were considered.

The blue-green OC4E algorithm [45, 46], given by,

$$\text{Chl-}a = 10^{0.368 - 2.814R_E + 1.456R_E^2 + 0.768R_E^3 - 1.292R_E^4}, \quad (6)$$

where,  $R_E = \log_{10}\left(\frac{\max(R_{443}, R_{490}, R_{510})}{R_{560}}\right)$  and  $R_x$  is the reflectance at the waveband centered at  $x$  nm.

Two-band NIR-red algorithm [32–34,47–49], given by,

$$\text{Chl-}a = A \times [R_{665}^{-1} \times R_{708}] + B, \quad (7)$$

where  $A$  and  $B$  were determined by regressing the ratio  $R_{708}/R_{665}$  with the chl-*a* concentrations in the *in situ* measured data set, and were set as 79.324 and −50.674, respectively.

Three-band NIR-red algorithm [32–34,48–50], given by,

$$\text{Chl-}a = A \times [(R_{665}^{-1} - R_{708}^{-1}) \times R_{753}] + B, \quad (8)$$

where  $A$  and  $B$  were determined by regressing the three-band ratio  $(R_{665}^{-1} - R_{708}^{-1}) \times R_{753}$  with the chl-*a* concentrations in the *in situ* measured data set, and were set as 253.11 and 29.74, respectively.

## 3. Results and discussion

### 3.1. Variations in SNR with changes in sensor configuration

As expected, SNR changes when the sensor configuration is changed as described in section 2.2. Figure 6 illustrates the changes in SNR as the blaze wavelength and the diameter of the aperture are changed. A change in the blaze wavelength causes a spectral shift in the magnitude of the SNR. The decision on the location of the blaze wavelength is driven by the intended use of the data retrieved from the sensor. Increasing the diameter of the aperture by decreasing the F-number raises the SNR across the spectral range independent of wavelength. On average, changing the blaze wavelength from 400 nm to 600 nm decreases the SNR-peak by about 15, changing the aperture size from 0.019 m to 0.024 m by decreasing the F-number from 3.5 to 2.8 increases the SNR-peak by about 50 (Table 4). Table 4 contains estimated errors in the retrieved constituent concentrations for various sensor configurations.

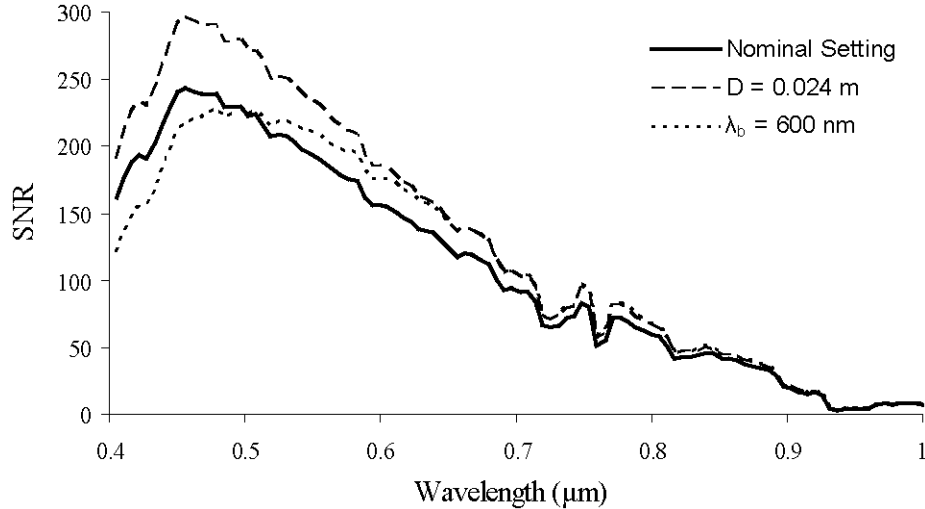


Fig. 6. Variations in at-sensor SNR as the sensor configuration is changed, for a case with chl-*a* = 2.27 mg m<sup>-3</sup>,  $a_{\text{CDOM}}(440)$  = 1.35 m<sup>-1</sup>, and TSS = 1.19 g m<sup>-3</sup>. The solid black line represents the SNR for nominal sensor setting (the blaze wavelength,  $\lambda_b$  = 400 nm; diameter of the aperture, D = 0.019 m).

### 3.2. Spectral effect of noise in the retrieved reflectance

Each of the noise-added atmospherically corrected spectra was compared with the corresponding original at-surface Rrs spectrum and quasi-SNR values were calculated by taking the root mean square error of the noise-added atmospherically corrected Rrs spectra as a measure of noise.

$$\text{Quasi-SNR}(\lambda) = \frac{R_{\text{orig}}(\lambda)}{\sqrt{\frac{1}{1000} \sum_{i=1}^{1000} (R_{\text{noise}}(\lambda)_i - R_{\text{orig}}(\lambda))^2}}, \quad (9)$$

where  $R_{\text{orig}}(\lambda)$  is the original at-surface Rrs at wavelength  $\lambda$  and  $R_{\text{noise}}(\lambda)_i$  is the noise-added Rrs at wavelength  $\lambda$  for the  $i^{\text{th}}$  pixel. The quasi-SNR( $\lambda$ ) values varied depending on the magnitude of the radiance from the target. CDOM absorbs light strongly in the blue region. Therefore, high concentrations of CDOM produce low magnitudes of reflectance in the blue region, resulting in low levels of quasi-SNR in the blue region (Fig. 7). Conversely, high concentrations of sediments produce increased scattering of light, which increases the magnitude of reflectance, thereby increasing the quasi-SNR and consequently reducing the impact of photon noise on the retrieved reflectance. An understanding of the expected levels of SNR in different spectral regions will help in the choice of spectral algorithms for retrieving constituent concentrations.

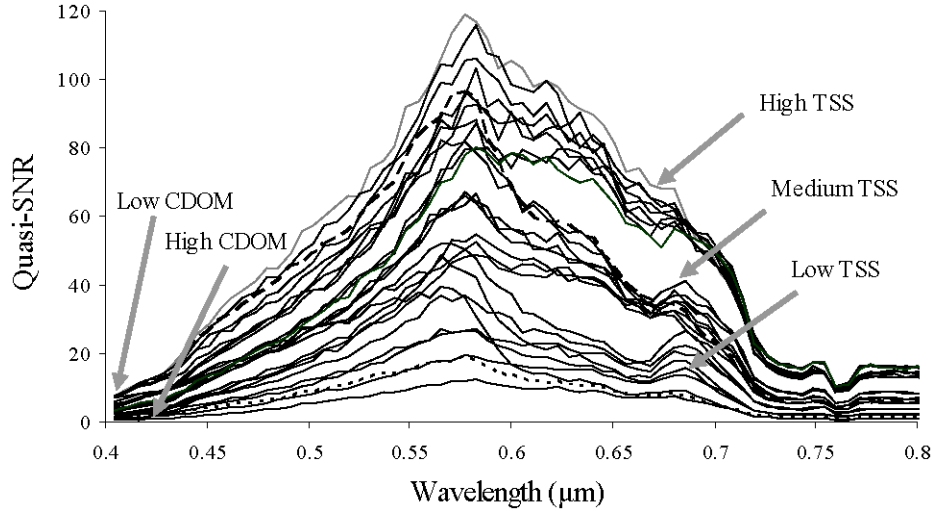


Fig. 7. Quasi-SNR of the noise-added atmospherically corrected Rrs spectra with the nominal sensor setting. High CDOM concentration causes low quasi-SNR, especially in the blue region, whereas high TSS concentration causes high quasi-SNR throughout the spectrum.

### 3.3. Estimation of constituent concentrations

#### 3.3.1. Estimates from the optimized error minimization approach

Estimates of constituent concentrations from each of the noise-added (based on nominal HICO sensor configuration) atmospherically corrected spectra were compared with the true concentrations corresponding to the original Rrs spectra. For the sake of brevity, only the results for the nominal HICO sensor configuration are shown in the figures. Table 4 contains the error estimates for various sensor configurations. The normalized root mean square errors were calculated as,

$$\text{Norm\_RMSE\_Chl} = \frac{\sqrt{\frac{1}{1000} \sum_{i=1}^{1000} (\text{Chl\_noise}_i - \text{Chl\_orig})^2}}{\text{Chl\_orig}} \quad (10)$$

$$\text{Norm\_RMSE\_TSS} = \frac{\sqrt{\frac{1}{1000} \sum_{i=1}^{1000} (\text{TSS\_noise}_i - \text{TSS\_orig})^2}}{\text{TSS\_orig}} \quad (11)$$

$$\text{Norm\_RMSE\_CDOM} = \frac{\sqrt{\frac{1}{1000} \sum_{i=1}^{1000} (a_{\text{CDOM}}(440)\text{-noise}_i - a_{\text{CDOM}}(440)\text{-orig})^2}}{a_{\text{CDOM}}(440)\text{-orig}}, \quad (12)$$

**Table 4.** The magnitude of SNR-peak (SNR<sub>peak</sub>), the location of SNR-peak (SNR<sub>peak wl</sub>) in nm, and the percent normalized RMSEs of chl-*a* concentration (%NR<sub>Chl-*a*</sub>), CDOM absorption (%NR<sub>CDOM(440)</sub>), and TSS concentration (%NR<sub>TSS</sub>) estimated by the optimized error minimization approach at low ( $a_{CDOM}(440) = 0.1 \text{ m}^{-1}$ ) and high ( $a_{CDOM}(440) = 2 \text{ m}^{-1}$ ) concentrations of CDOM for various sensor configurations. The blaze wavelength was kept at 400 nm for sensor configurations with the nominal setting and  $D = 0.024 \text{ m}$ , and the peak SNR was achieved at 457 nm

Constituent Concentrations			Nominal Setting				$D = 0.024 \text{ m}$				$\lambda_b = 600 \text{ nm}$				
Chl- <i>a</i> (mg m <sup>-3</sup> )	$a_{CDOM}(440)$ (m <sup>-1</sup> )	TSS (g m <sup>-3</sup> )	SNR <sub>peak</sub>	%NR <sub>Chl-<i>a</i></sub>	% NR $a_{CDOM}(440)$	%NR <sub>TSS</sub>	SNR <sub>peak</sub>	%NR <sub>Chl-<i>a</i></sub>	% NR $a_{CDOM}(440)$	%NR <sub>TSS</sub>	SNR <sub>peak</sub>	%NR <sub>Chl-<i>a</i></sub>	% NR $a_{CDOM}(440)$	%NR <sub>TSS</sub>	
2	0.1	1	246	31	13	10	299	27	12	9	231	497	40	17	13
2	0.1	4	250	42	18	3	303	35	15	2	238	508	53	23	4
2	0.1	8	251	49	22	1	306	41	18	1	242	508	61	28	1
2	0.1	14	252	45	22	1	307	38	19	1	246	577	53	27	1
2	0.1	20	253	38	22	1	308	32	18	1	252	583	43	26	1
15	0.1	1	245	14	22	15	298	12	18	12	231	497	17	28	18
15	0.1	4	248	15	26	3	301	13	22	3	235	508	19	33	4
15	0.1	8	250	16	28	1	304	14	24	1	239	508	20	35	2
15	0.1	14	251	15	28	1	305	13	24	1	242	577	18	35	1
15	0.1	20	252	12	26	1	306	11	23	1	248	583	14	31	1
25	0.1	1	245	11	25	16	298	10	21	13	230	497	14	33	20
25	0.1	4	247	13	30	4	301	11	25	3	234	508	16	38	5
25	0.1	8	249	13	31	1	303	11	26	1	238	508	16	39	2
25	0.1	14	251	12	31	1	305	10	26	1	241	508	14	38	1
25	0.1	20	251	10	31	1	306	9	25	1	246	583	11	36	1
50	0.1	1	245	9	33	19	298	8	28	16	230	497	12	45	25
50	0.1	4	247	10	37	4	300	8	31	4	233	508	12	47	5
50	0.1	8	248	10	38	2	302	8	32	2	236	508	12	46	2
50	0.1	14	250	8	36	1	304	7	30	1	239	508	10	44	1
50	0.1	20	250	7	35	1	305	6	30	1	243	577	8	43	1
2	2	1	239	79	11	32	290	71	9	28	222	479	80	11	33
2	2	4	240	78	4	6	292	67	3	5	224	479	79	4	6
2	2	8	242	63	2	2	294	55	2	2	227	497	60	2	2
2	2	14	244	46	2	1	296	40	2	1	230	508	44	2	1
2	2	20	245	37	2	1	298	32	2	1	233	508	35	2	1
15	2	1	239	26	7	33	291	23	6	29	223	479	26	8	35
15	2	4	241	24	4	6	292	21	3	5	225	479	24	4	6
15	2	8	242	19	3	2	294	17	2	2	227	497	20	3	2
15	2	14	244	15	2	1	296	13	2	1	230	508	14	2	1
15	2	20	245	13	2	1	298	11	2	1	233	508	12	2	1
25	2	1	240	21	7	35	291	18	5	30	224	479	21	7	37
25	2	4	241	19	4	7	292	16	3	6	225	479	20	4	7
25	2	8	242	16	3	2	294	13	2	2	227	497	15	3	2
25	2	14	244	11	2	1	296	10	2	1	230	508	11	2	1
25	2	20	245	10	2	1	298	9	2	1	233	508	9	2	1
50	2	1	240	16	6	38	292	13	5	31	224	479	16	7	40
50	2	4	241	13	4	7	293	12	3	6	226	479	14	4	7
50	2	8	242	11	3	3	294	9	3	2	227	497	11	3	3
50	2	14	244	8	3	1	296	7	2	1	230	508	8	3	1
50	2	20	245	8	2	1	297	6	2	1	232	508	7	2	1

where  $X_{noise_i}$  is the constituent concentration at the  $i^{\text{th}}$  pixel of the noise-added atmospherically corrected image and  $X_{\text{orig}}$  is the true constituent concentration of the original Rrs spectrum.

Variations up to 80% were observed in the estimated chl-*a* concentration due to photon noise (Fig. 8), especially in cases of high concentration of CDOM and low concentrations of TSS and chl-*a*. At low-to-moderate concentrations of chl-*a* and TSS, the presence of CDOM enhanced the variations in estimated chl-*a* concentrations due to photon noise. As the concentrations of TSS and chl-*a* increased, the effect of CDOM on the variations in estimated chl-*a* concentrations diminished, and the variations in chl-*a* estimation decreased to around 15% or less.

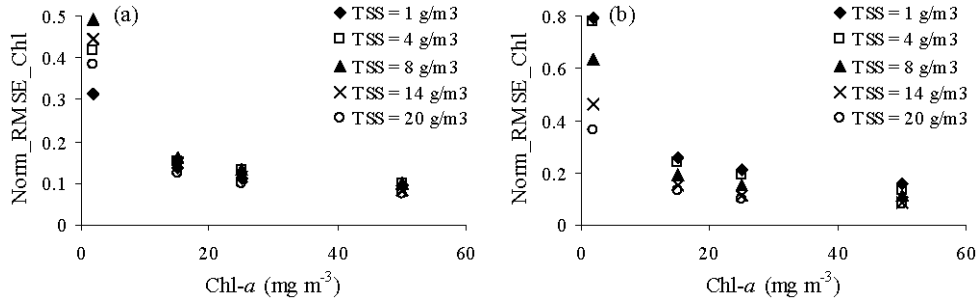


Fig. 8. Normalized RMSE of estimated chl-*a* concentrations (by the optimized error minimization approach) for (a)  $a_{CDOM}(440) = 0.1\ m^{-1}$  and (b)  $a_{CDOM}(440) = 2\ m^{-1}$  at various TSS concentrations.

CDOM had a similar effect on the variations in the estimated TSS concentrations also (Fig. 9). Increase in TSS concentration produced a decrease in the variations of the estimated  $a_{CDOM}(440)$  values (Fig. 10) due to sensor noise except at very low concentrations of CDOM, where increased scattering due to TSS masks the CDOM absorption feature in the blue region, which is already small at low concentrations of CDOM.

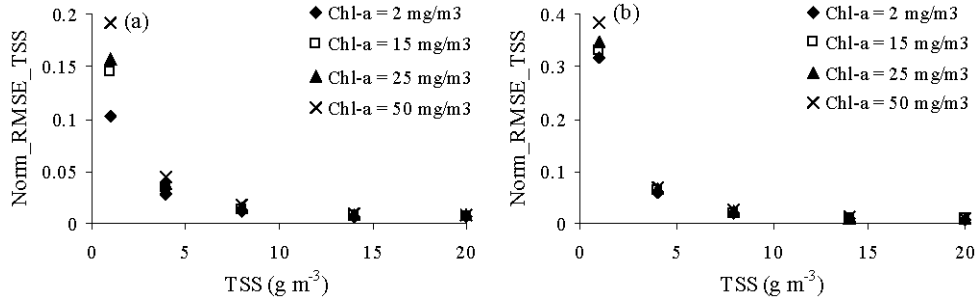


Fig. 9. Normalized RMSE of estimated TSS concentrations (by the optimized error minimization approach) for (a)  $a_{CDOM}(440) = 0.1\ m^{-1}$  and (b)  $a_{CDOM}(440) = 2\ m^{-1}$  at various chl-*a* concentrations.

Increasing the diameter of the aperture to 0.024 m resulted in a reduction in the variations in the estimated chl-*a* concentration, with the improvement more pronounced at low concentrations of chl-*a* and TSS (Fig. 11). Changing the blaze wavelength to 600 nm had a negligible effect on the estimated chl-*a* concentration when the CDOM concentration was high. But when the CDOM concentration was low, changing the blaze wavelength to 600 nm resulted in an increase in the variations, especially at low chl-*a* concentration, where the sensitivity of the sensor to the absorption by chl-*a* in the blue region plays a critical role.

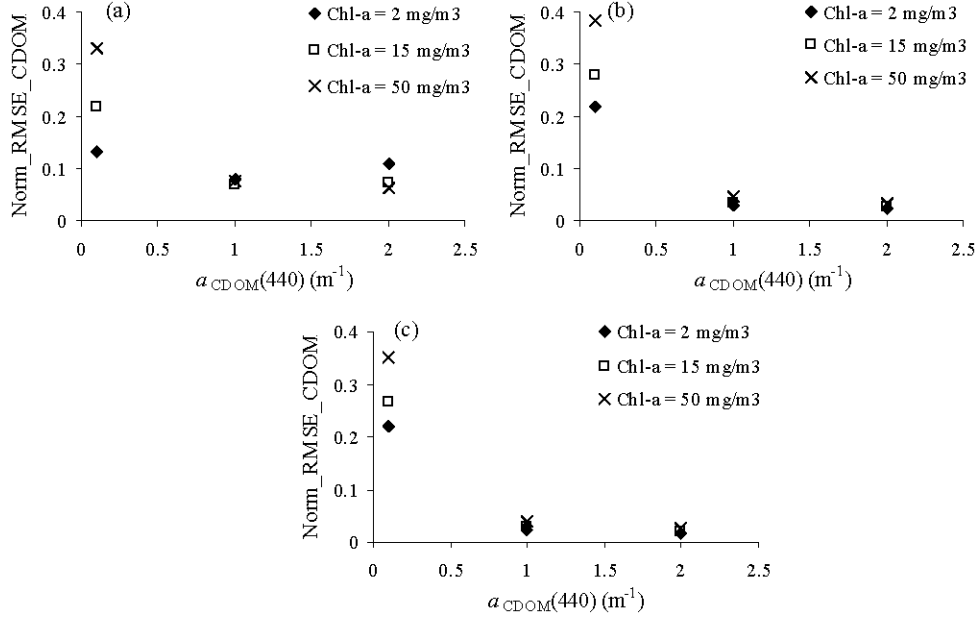


Fig. 10. Normalized RMSE of estimated  $a_{CDOM}(440)$  (by the optimized error minimization approach) for (a) TSS =  $1 \text{ g m}^{-3}$ , (b) TSS =  $8 \text{ g m}^{-3}$ , and (c) TSS =  $20 \text{ g m}^{-3}$  at various chl- $a$  concentrations.

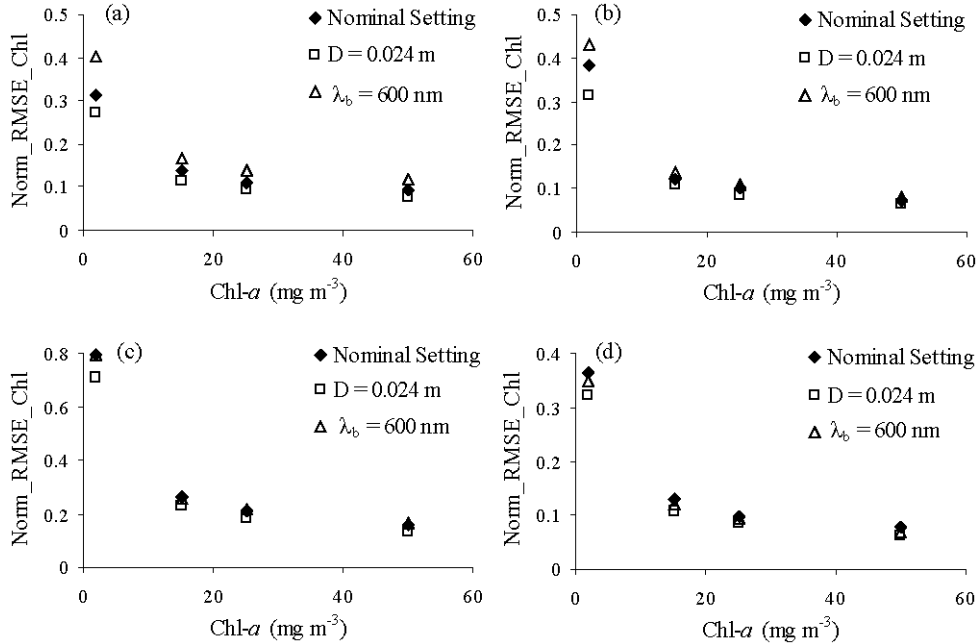


Fig. 11. Normalized RMSE of estimated chl- $a$  concentrations (by the optimized error minimization approach) for various sensor configurations at low and high concentrations of TSS and CDOM: (a) TSS =  $1 \text{ g m}^{-3}$  and (b) TSS =  $20 \text{ g m}^{-3}$  with  $a_{CDOM}(440) = 0.1 \text{ m}^{-1}$ ; (c) TSS =  $1 \text{ g m}^{-3}$  and (d) TSS =  $20 \text{ g m}^{-3}$  with  $a_{CDOM}(440) = 2 \text{ m}^{-1}$ .

Changing the aperture size and the blaze wavelength produced similar effects on the estimated TSS concentrations as for the estimated chl- $a$  concentrations.

In general, for all sensor configurations, variations due to photon noise were higher in the estimates of chl-*a* concentration than in the estimates of TSS concentration and  $a_{CDOM}(440)$ , which is consistent with the results obtained by Levin and Levina [51].

### 3.3.2. Estimates from semi-analytical algorithms

The semi-analytical algorithms considered in this study were originally developed for use with data from the multispectral sensor, MERIS. Therefore, MERIS images were simulated from the HICO-based noiseless as well as noise-added atmospherically corrected images based on the central wavelength locations and the full width at half maximum of the spectral channels of MERIS. Chl-*a* concentrations were calculated from the noiseless images using each of the semi-analytical algorithms and were used as the standard against which the chl-*a* concentrations estimated from the noise-added image by these algorithms were compared. The normalized root mean square errors of chl-*a* estimation were calculated in the same manner as in Eq. (10), with Chl\_orig substituted by the respective chl-*a* concentration estimated from the noiseless image.

#### 1. OC4E algorithm

When compared to the chl-*a* concentrations calculated from noiseless images, the estimated chl-*a* concentrations varied by an average of more than 15% due to photon noise for the nominal sensor setting (Fig. 12). Increasing the diameter of the aperture to 0.024 m reduced the average variation to 13.4%. The blaze wavelength was adjusted in steps of 50 nm from 400 nm to 600 nm. The changes in the relative errors of estimated chl-*a* concentration were minor (< 1% on average), with the best results obtained when the blaze wavelength was set at the blue-green wavelength, 500 nm. When the blaze wavelength was set at 500 nm and the diameter of the aperture at 0.024 m simultaneously, the relative error in the estimated chl-*a* concentration decreased to ~12.75%.

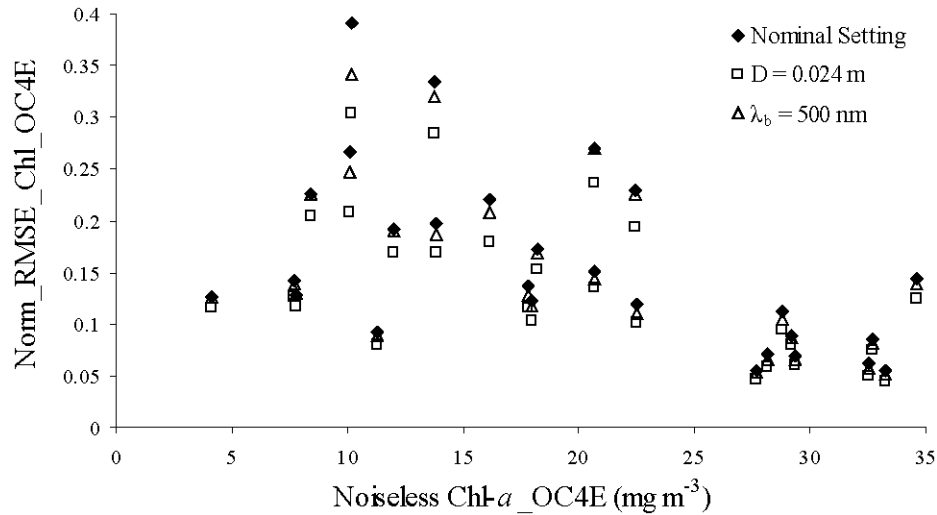


Fig. 12. Normalized RMSE of chl-*a* concentrations estimated by the OC4E algorithm.

#### 2. Two-band NIR-red algorithm

Due to low reflectance of water in the NIR region, the two-band NIR-red algorithm is quite vulnerable to the effects of photon noise in the 708 nm band. This is especially pronounced when the concentrations of chl-*a* and TSS are low, resulting in very low magnitudes of reflectance in the 708 nm band. The algorithm relies significantly on the reflectance peak around 708 nm, which is quite sensitive to chl-*a* concentration [47].

Therefore at low chl- $a$  concentrations, when the reflectance at 708 nm is low, the two-band NIR-red algorithm is very susceptible to photon noise.

With the nominal sensor setting, relative errors in estimated chl- $a$  concentrations reached as high as 80% (Fig. 13(a)) for low chl- $a$  concentrations, excluding three stations with chl- $a$  concentration less than  $5 \text{ mg m}^{-3}$ , for which about 50% of the pixels had invalid reflectances in the NIR region due to photon noise and were hence excluded. The average relative error in the estimated chl- $a$  concentration was 19.23%. Increasing the diameter of the aperture to 0.024 m reduced the relative error to 17.54%, whereas changing the blaze wavelength to 600 nm reduced the relative error to 17.43%. When chl- $a$  concentrations less than  $15 \text{ mg m}^{-3}$  were omitted, the relative error for the nominal sensor setting was 10.96%, and the aforementioned changes in the aperture size and the blaze wavelength produced relative errors of 9.74% and 9.7%, respectively.

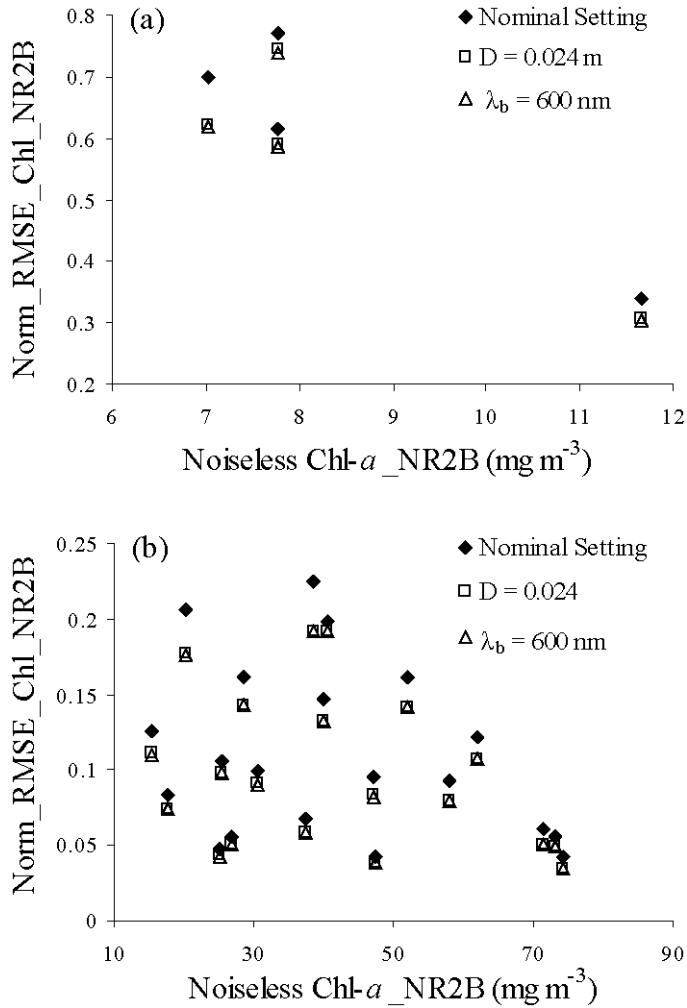


Fig. 13. Normalized RMSE of chl- $a$  concentrations estimated by the two-band NIR-red algorithm for (a) low and (b) moderate-to-high chl- $a$  concentrations.

### 3. Three-band NIR-red algorithm

Similar results were obtained for the three-band NIR-red algorithm (Fig. 14) as with the two-band NIR-red algorithm. Variations in the estimated chl- $a$  concentrations due to photon noise were high for low chl- $a$  concentrations. Excluding three stations because of the high

percentage of pixels ( $> 50\%$ ) with invalid reflectances in the NIR wavebands at 708 nm and 753 nm, the relative error in the estimated chl- $a$  estimation for the nominal sensor setting was 19.11%, which decreased to 17.38% and 17.21%, respectively, as the diameter of the aperture was increased to 0.024 m and the blaze wavelength changed to 600 nm. When chl- $a$  concentrations less than  $15 \text{ mg m}^{-3}$  were omitted, the relative errors were 10.67% for the nominal setting, 9.54% for  $D = 0.024 \text{ m}$  and 9.49% for  $\lambda_b = 600 \text{ nm}$ .

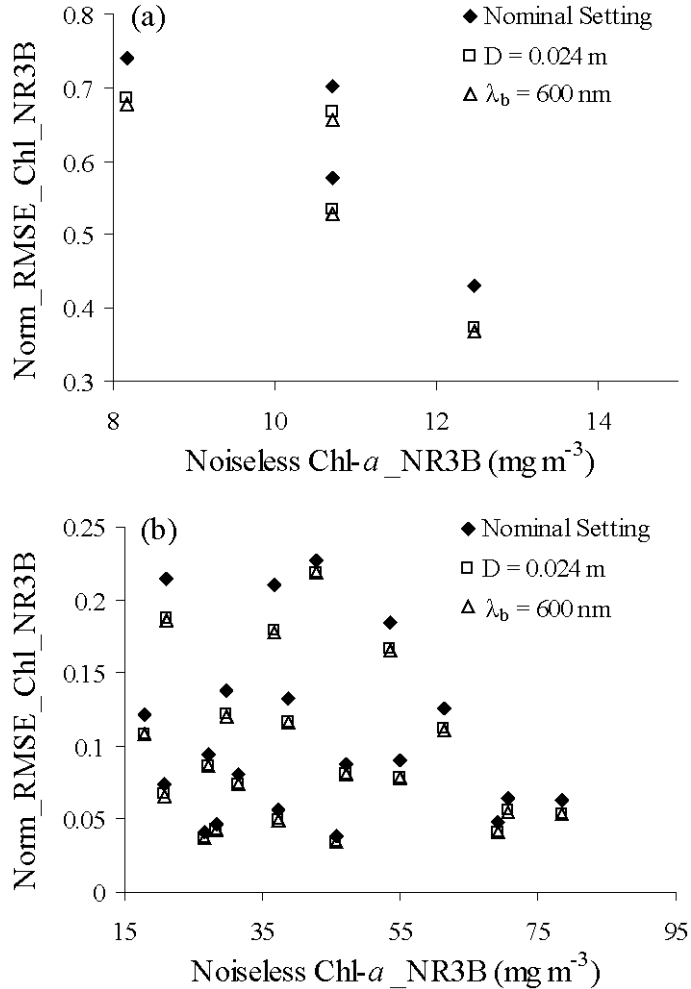


Fig. 14. Normalized RMSE of chl- $a$  concentrations estimated by the three-band NIR-red algorithm for (a) low and (b) moderate-to-high chl- $a$  concentrations.

#### 4. Conclusion

The results indicate that even in “best possible” conditions the photon noise in the sensor alone can result in errors at the level of 50% or more in the retrieved constituent concentrations. The error is particularly significant for waters with high levels of CDOM and low-to-moderate concentrations of chl- $a$  and TSS, where errors as high as 80% or more are attributable to uncertainties in the retrieved reflectance due to photon noise. The magnitude of the effect of photon noise can be controlled by adjusting the sensor configuration. Increasing the aperture size and/or changing the blaze wavelength can improve the accuracy of estimated constituent concentrations by a few percentage points. The suggestion here is not that it is unnecessary or impossible to further improve the bio-optical algorithms for retrieving

constituent concentrations from spaceborne remotely sensed data. On the contrary, some improvements to the algorithms can be made. In the optimized error minimization approach, for example, weighting the wavelengths specific to the spectral features of interest (for instance, the chl-*a* absorption feature around 440 nm or 670 nm) may produce improved results. However, even then the general behavior shown here will still persist. In other words, the observed errors due to photon noise will be present even in the case of a perfect bio-optical algorithm as long as the algorithm relies on retrieved reflectances. Thus, the quantitative effects of uncertainties due to photon noise need to be considered when assessing the accuracies yielded by bio-optical algorithms.

The results presented here are for a best case scenario. Errors due to imperfect radiometric calibration of the sensor have not been considered. Only the nadir viewing angle (ensuring the lowest amount of atmosphere possible) is considered. Sun glint is ignored. It is assumed that the atmosphere is perfectly known and the atmospheric effects are perfectly removed. In a real scenario, these aforementioned effects and others that are hard to recognize and/or repair will contribute to further errors in the retrieved constituent concentrations, and the sensitivity of these effects to the sensor's SNR needs to be investigated in order to get a comprehensive understanding of the uncertainties in the retrieved constituent concentrations.

### Acknowledgments

This research was supported by the Office of Naval Research and by the National Research Council Associateship awarded to W. J. Moses via the Naval Research Laboratory.